Journal of Materials Chemistry A

ROYAL SOCIETY OF CHEMISTRY

PAPER

View Article Online
View Journal | View Issue

Check for updates

Cite this: J. Mater. Chem. A, 2022, 10, 10171

Ultra-high energy density integrated polymer dielectric capacitors†

Xintong Ren, [a] Nan Meng, [ab] Leonardo Ventura,[a] Stergios Goutianos,[c] Ettore Barbieri,[d] Han Zhang, [ae] Haixue Yan, [ae] Michael John Reece*[ae] and Emiliano Bilotti *[ae]

Received 20th October 2021
Accepted 24th March 2022

DOI: 10.1039/d1ta09045c

rsc.li/materials-a

Flexible dielectric polymers with high energy storage density are needed for film capacitor applications including hybrid electric vehicles and medical apparatuses. Poly(vinylidene fluoride) (PVDF) is regarded as a promising candidate owing to its intrinsic high polarisation, outstanding processability, good mechanical properties, and high dielectric breakdown strength. However, normal PVDF suffers from low energy density (U_e) and charge–discharge efficiency (η) at high electric fields. In this study, these restrictions are successfully overcome using a novel facile one-step Roll & Press method. A record high energy storage density of 50.2 J cm^{-3} with an outstanding charge–discharge efficiency of 80% is achieved at 1000 kV mm^{-1} in relaxor-like PVDF, which is ascribed to reversible polar nanostructures generated by the constraining effect originating from continuous folded boundaries in the multilayer structure during rolling and pressing. The superior energy storage performance of Roll & Pressed PVDF surpasses those of all other polymer-based materials reported. Additionally, a ready-to-use capacitor is assembled using the Roll & Press technique with electrodes constructed using a stretchable carbon nanotube veil (CNT veil), which exhibits strong interfacial interactions with the PVDF film and results in excellent energy storage performance. The universal applicability of the Roll & Press method and superior energy storage properties makes PVDF a strong candidate for modern energy storage systems.

1. Introduction

Flexible polymer dielectric capacitors with an ultrafast charge–discharge speed, high energy density (U_e), and efficiency (η) are of great importance for the next generation of hybrid electric vehicles, pulsed power systems and medical apparatus.[1–4] The state-of-the-art material for commercial capacitors, biaxially oriented polypropylene (BOPP), exhibits a low permittivity ε_r (~2.3 at 1 kHz) and a low discharged energy density U_e (~4 J cm^{-3} at 650 kV mm^{-1}).[5–7] One strategy to overcome the low U_e of BOPP is to use relaxor polymers including local polar structures.[8–10] PVDF possesses a unique polar structure –(CH_2–CF_2)$_n$–, giving rise to a large dipole moment of 7×10^{-30} C m (~2.1 Debye, 1 Debye = 3.33564×10^{-30} C m) pointing from the more electronegative fluorine (electronegativity $\chi = 3.98$) to the hydrogen ($\chi = 2.20$).[11,12] Owing to its intrinsic high polarisation and an all-trans chain conformation, β-phase PVDF (space group: *Cm2m*) displays desirable dielectric (ε_r: ~10–12 at 1 kHz), piezoelectric (piezoelectric coefficient d_{33}: ~20–30 pC N^{-1}), and ferroelectric (spontaneous polarisation P_s: 0.13 C m^{-2}) properties,[4,13] which have been extensively explored for applications in piezoelectric sensors, non-volatile memory devices, and electrostrictive actuators.[14–16] However, utilizing β-PVDF in high-power dielectric capacitors is limited due to its high dielectric displacement at zero field D_r (~0.075 C m^{-2} at 300 kV mm^{-1}), originating from irreversible dipole rotation during ferroelectric switching, which results in a low charge–discharge efficiency (~35%).[17,18]

To overcome the limitation of low η in ferroelectric β-PVDF, relaxor ferroelectric terpolymers P(VDF-TrFE-CTFE/CFE) (TrFE: trifluoroethylene; CFE: chlorofluoroethylene; CTFE: chlorotrifluoroethylene) with highly reversible polar nanodomains have been developed. However, the commercialization of dielectric capacitors using relaxor ferroelectric polymers is still hindered by their low dielectric breakdown strength, high cost, and low throughput during processing. Apart from commercial

[a]School of Engineering and Materials Science, Queen Mary University of London, Mile End Road, E1 4NS, London, UK. E-mail: e.bilotti@qmul.ac.uk; m.j.reece@qmul.ac.uk
[b]State Key Laboratory for Modification of Chemical Fibers and Polymer Materials, College of Materials Science and Engineering, Donghua University, Shanghai, 201620, China
[c]Department of Manufacturing and Civil Engineering, Norwegian University of Science and Technology, 2821 Gjøvik, Norway
[d]Japan Agency for Marine-Earth Science and Technology, Research Institute for Value-Added-Information Generation (VAiG), Center for Mathematical Science and Advanced Technology (MAT), 3173-25, Showa-machi, Kanazawa-ku, Yokohama-city, Kanagawa, 236-0001, Japan
[e]NPU-QMUL Joint Research Institute of Advanced Materials and Structure (JRI-AMAS), Northwestern Polytechnical University, 710072, Xi'an, China

† Electronic supplementary information (ESI) available. See DOI: 10.1039/d1ta09045c

considerations, understanding the origin of the relaxor ferroelectricity of PVDF-based copolymers and terpolymers provides useful information for designing new materials. It is believed that relaxor ferroelectricity arises from the broadened intermolecular chain distance and defects in bulk chlorinated monomer/irradiation induced crosslinking, which interrupts the long-range all-trans molecular chain conformation and transforms the ferroelectric domains into polar nanodomains.[19–21] Recently, a novel processing method "Press & Fold" was developed to enhance the U_e and η by using internal strain engineered highly reversible polar nanostructures.[18,22] If high internal strain is key to achieving superior energy storage performance, there may be even more efficient mechanical loading approaches. It was, for instance, observed that mechanically constrained (folded) boundaries during pressing play a critical role in achieving higher fractions of β phase, due to a more efficient stress transfer (Fig. S1†).

Herein we present a new processing method, called Roll & Press, that achieves relaxor-like ferroelectricity with high U_e and η in a single pressing step, which outperforms Press & Fold in terms of production efficiency (120 min for Press & Fold *vs.* 20 min for Roll Press), energy sustainability (6 cycles *vs.* 1 cycle), and possibility of simultaneously embedding electrodes during processing. In brief, when a PVDF film is rolled on itself and pressed, a large internal stress is built up in the film when the temperature is first increased (up to slightly below the melting temperature) and then decreased (quenched) to a moderate temperature followed by an annealing treatment at the same temperature. We show that Roll & Press PVDF can achieve a giant recoverable energy density of 50.2 J cm^{-3} with a charge–discharge efficiency of 80% at 1000 kV mm^{-1}. To the best of our knowledge, this is the highest U_e with outstanding η reported among all polymer-based materials, which paves the way to the development of high-power density dielectric capacitors with high energy density. Compared with traditional uniaxial/biaxial stretching, Roll & Press surpasses with stable relaxor-like ferroelectricity (low D_r and high $D_{in\text{-}max}$) over a wide electric field range (up to 1000 kV mm^{-1}), which originates from its high β-phase content, small crystallite size, and high internal strain. Besides, Roll & Press is advantageous in producing high-quality thin films for high molecular weight polymers benefiting from its wide processing temperature range.[23–25] An additional benefit of the Roll & Press method is the possibility of incorporating electrodes, and hence fabricating a ready-to-use PVDF capacitor in one step, while preserving the relaxor-like ferroelectricity of Roll & Press PVDF. As a proof of concept, a carbon nanotube veil (CNT veil) was utilized as the electrode, owing to its light weight, outstanding stretchability under high pressure, and high electrical and thermal conductivity.[26,27]

2. Results and discussion

In order to investigate the most effective method to layer the films before pressing, layered films with a similar area (10 cm^2) and number of layers (10 layers) but different boundary conditions were prepared, namely "Stack & Press", "Zigzag & Press" and "Roll & Press" (Fig. 1a). All of these films were pressed at a pressing temperature T_p of 60 °C with a force of 300 kN (nominal pressure: 300 kN/10 cm^2 = 300 MPa). Then, the temperature was increased to a maximum temperature T_{max} of 165 °C without melting the film (melting temperature of the PVDF: 172 °C). Subsequently, the films were annealed at an annealing temperature T_{anneal} of 165 °C for 10 minutes. Finally, the films were quenched using cold water to room temperature and then the pressure was removed. As shown in Fig. S1a,† three free boundaries and one folded boundary are generated between two adjacent layers when a film is folded once. In the stacked film, where there is no folding, all four boundaries between two adjacent layers are free boundaries without any constraint. There are one and two folded boundaries in the zigzagged and the rolled film, respectively. The films with a similar initial area but folded boundaries exhibited more plastic deformation and a larger increase in the area after pressing once: ~530% and ~450% for Zigzag & Pressed and Roll & Pressed films respectively, compared with ~400% for the Stack & Pressed film with free edges (Fig. S2†). This is consistent with the FEM simulation results in Fig. 1b, where the highest plastic deformation strain was observed at the folded boundary in the Roll & Press film. The highest average plastic deformation strain was observed in the Zigzag & Press film while the Stack & Press film showed the lowest deformation strain. The finite element simulated responses of the films when pressure was exerted on them are shown in supplemental videos, which are more intuitive for displaying the plastic deformation (ESI videos 1–3†). According to the FTIR and XRD results in Fig. 1c and d, Roll & Press (fraction of β phase $F(\beta)$: 80 ± 8% after pressing) is the most effective approach to transform the non-polar α phase (Fig. 1c and d, powder and hot-pressed PVDF) into the polar β phase, which could be attributed to the larger plastic deformation demonstrated above. As an additional confirmation of the important role played by the folded boundaries, the Roll & Press PVDF film also exhibited the highest internal strain of 2.1 ± 0.2% compared with 0.1 ± 0.1% for the Stack & Press film and 0.6 ± 0.1% for the zigzag film, as calculated from the shift of the $(110)/(200)_\beta$ diffraction peak (Fig. S3a†).

To achieve a higher α to β phase transformation, a thinner (<20 μm) free-standing film, and a better understanding of the Roll & Press process, a more detailed study with three different rolling conditions was conducted (Fig. 1e). ΔC_h is defined as the difference of circumference between the current semicircle and the previous semicircle during rolling. ΔC_h is 0 mm for a tightly rolled film. Loosely rolled films (ΔC_h = 3 mm and ΔC_h = 5 mm) were assembled and pressed using identical pressing conditions to those for the tightly rolled films. All of the films after rolling had an area of 10 cm^2 before pressing and a layer number of 10. The highest $F(\beta)$ of 90 ± 6% was obtained in the Roll & Press films with ΔC_h = 3 mm, suggesting that a balance exists between the constraining effect and the flowability of the material in order to maximize the phase transformation (Fig. 1f and g). A similar internal strain (2.1 ± 0.1%) was developed for the Roll & Press films with ΔC_h = 3 mm and the tightly rolled film (ΔC_h = 0 mm), suggesting that the constraining effect of the continuous folded boundaries was similarly effective (Fig. S3b†).

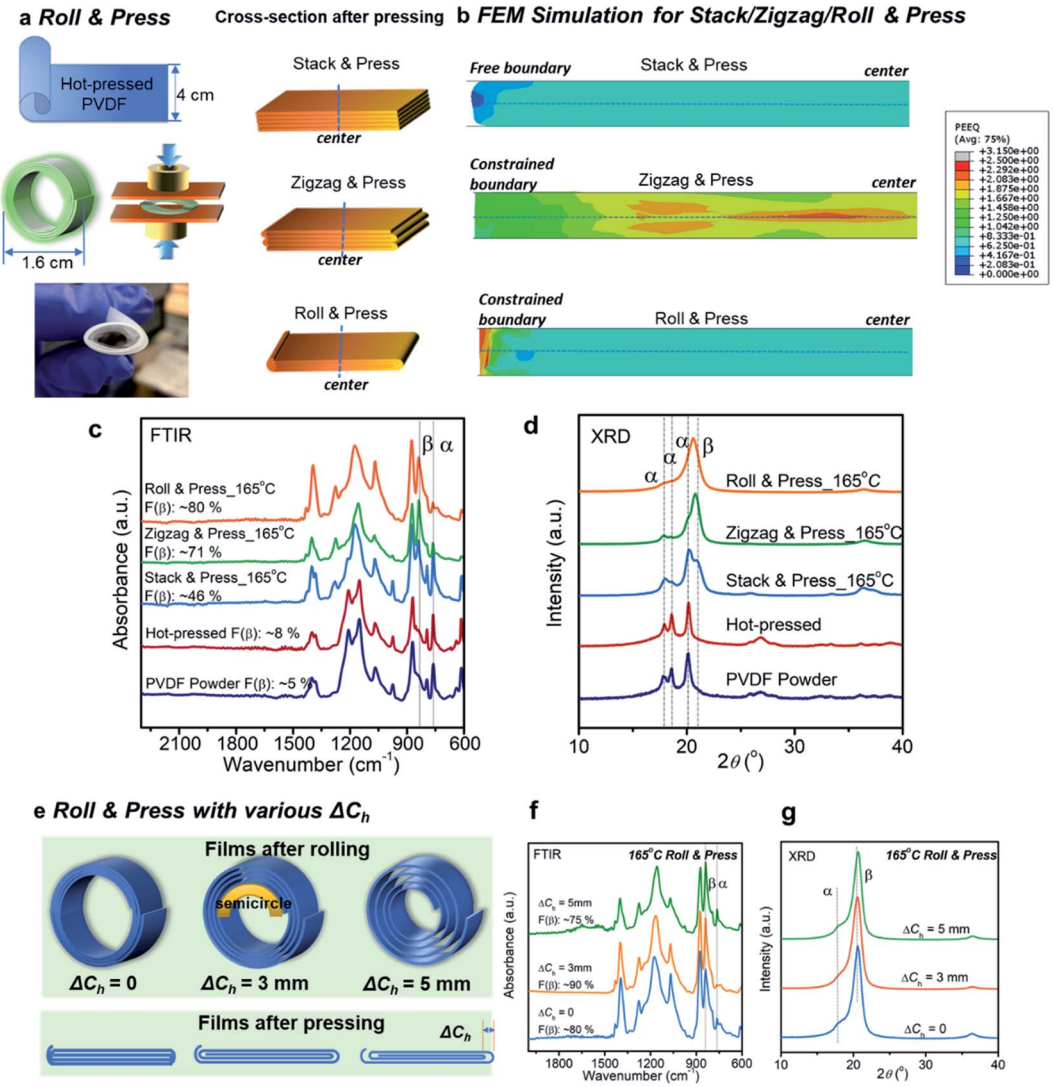

Fig. 1 a) Schematics of Stack & Press, Zigzag & Press, and Roll & Press. (b) FEM simulations of plastic deformations for PVDF films assembled with various boundary conditions. Due to symmetry, a domain corresponding to two half-layers of each film (denoted with dotted lines in the figure) is modelled. The scale bar represents the equivalent plastic strain of the films. (c) FTIR; (d) XRD patterns of PVDF powder, hot-pressed PVDF film, and multilayer films prepared at 165 °C using Stack & Press, Zigzag & Press and Roll & Press. (e) Schematic diagram of tightly rolled and loosely rolled PVDF with different ΔC_h after rolling and pressing, respectively. (f) FTIR; (g) XRD patterns of Roll & Press films with a ΔC_h of 0, 3 mm and 5 mm, respectively.

The *D*–*E* and *I*–*E* loops (Fig. S4†), at high electric fields (280 kV mm^{-1}), of all of the Roll & Press films showed unstable relaxor-like ferroelectricity as the backward poling current peak E_B and E'_Bshifted from the 4th/2nd quadrants to the 3rd/1st quadrants with decreasing (for E_B)/increasing (for E'_B) electric field and tended to merge with current peaks E'_F and E_F, respectively (Fig. S4a†). Comparatively, the Roll & Press film with a ΔC_h of 3 mm displayed the lowest $|E_F–E_B|$ (or $|E'_B - E'_F|$) among the Roll & Press films with different ΔC_h, indicating easier reversal of the field aligned dipoles because of its relatively higher internal strain (2.1 ± 0.1%) and $F(\beta)$ (90 ± 6%) than the Roll & Press film with a ΔC_h of 0 mm (internal strain: 2.1 ± 0.2%; $F(\beta)$: 80 ± 8%) and a ΔC_h of 5 mm (internal strain: 1.4 ± 0.1%; $F(\beta)$: 75 ± 7%). However, a higher internal strain is needed to further stabilize the reversible polar nanostructure and relaxor-like ferroelectricity at high electric fields.

Apart from the boundary conditions and pressure, the selection of the processing temperature of the Roll & Press procedure is also important. In particular, three processing temperatures should be highlighted: the press temperature T_p, the maximum temperature T_{max}, and the annealing temperature T_{anneal} (Fig. 2a). To generate stable relaxor-like ferroelectric behaviour in Roll & Press films, the effect of these temperatures on the phase transformation and ferroelectric properties was systematically studied (Fig. 2b–e). The applied pressure was ~300 MPa for all films. At least 10 samples were measured using FTIR to reveal the homogeneity of the films. Firstly, T_{max} was maintained at 165 °C to avoid melting the film, while a series of T_p were selected to perform the "press". With increasing T_p

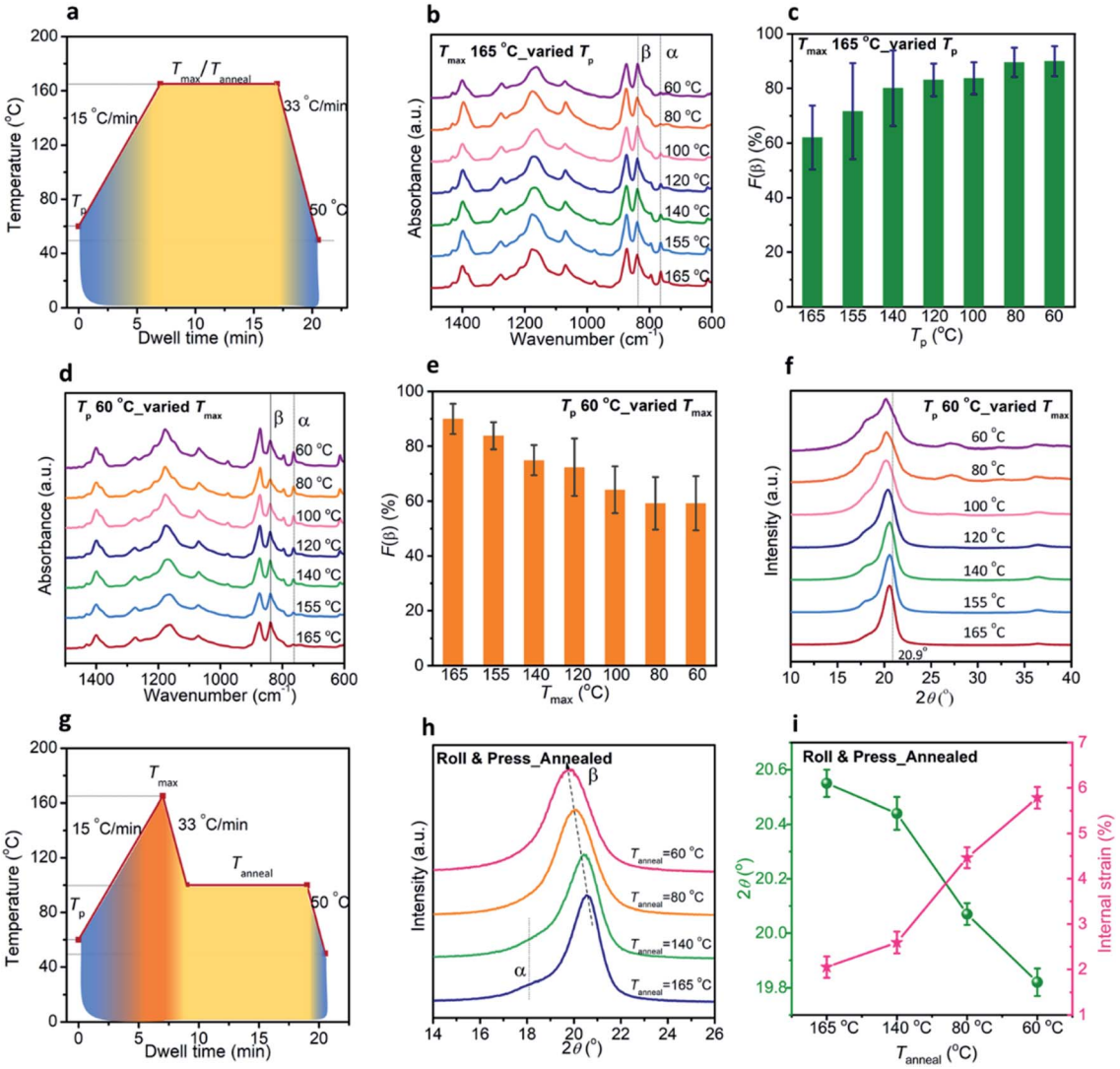

Fig. 2 a) Schematic diagram of the temperature procedure during Roll & Press with the three important temperatures T_p, T_{max} and T_{anneal} marked. (b) FTIR spectra; (c) $F(\beta)$ of the Roll & Press film with a ΔC_h of 3 mm prepared at a T_{max} of 165 °C with T_p varying from 165 °C to 60 °C. (d) FTIR spectra; (e) $F(\beta)$; (f) XRD patterns of the Roll & Press film with a ΔC_h of 3 mm prepared at a constant T_p of 60 °C with T_{max} varying from 165 °C to 60 °C. (g) Schematic of Roll & Press followed by an annealing step at lower temperature. (h) XRD patterns; (i) the peak position shift of the $(110/200)_\beta$ crystalline plane at 20.98° 2θ and the calculated internal strain with respect to the T_{anneal} of the Roll & Press film with a ΔC_h of 3 mm prepared at a T_p of 60 °C and a T_{max} of 165 °C, followed by annealing at 165 °C, 140 °C, 80 °C and 60 °C.

from 60 °C to 165 °C, the $F(\beta)$ gradually reduced from 90 ± 6% to 62 ± 12%, with a large variation from sample to sample. This implies that the films pressed at high temperatures tended to become inhomogeneous in terms of the phase conversion. This could be ascribed to the relaxation of molecular chains at high temperature, which has also been reported in uniaxially stretched PVDF.[28,29] The reduced α–β transition rates at high temperatures can be attributed to the predominant role played by thermal energy at high temperature in the competition between heat (which favours the paraelectric α-phase with a lower potential energy of −6.03 kcal mol^{-1}) and mechanical stress (which promotes the highly ordered ferroelectric β-phase (potential energy: −5.73 kcal mol^{-1})).[30] These results are consistent with those of uniaxially stretched PVDF where lower α–β transition rates are observed at higher stretching temperatures, when stretched below the melting temperature.[12,31]

Another set of films were fabricated using a constant T_p of 60 °C with T_{max} varied between 60 °C and 165 °C. Intriguingly, although higher T_{max} was favourable for achieving a higher fraction of β phase (Fig. 2d and e), a higher internal strain was built up in the films prepared at lower T_{max}, as the diffraction peak of $(110/200)_\beta$ continuously shifted from 20.55° 2θ (internal strain: 2.1 ± 0.1%) to 20.12° 2θ (internal strain: 4.3 ± 0.1%) when the T_{max} dropped from 165 °C to 60 °C. Therefore, the corresponding intermolecular chain distance experienced an expansion of 0.09 Å as calculated using Bragg's law. Deconvoluted XRD patterns and the Scherrer equation were utilized to calculate the average crystallite size and the internal strain of films Roll & Pressed at various T_{max}. As shown in Fig. S6a and

Table S1,† the average crystallite size reduced from 6.3 ± 0.2 nm for the film prepared at a T_{max} of 165 °C to 3.8 ± 0.2 nm for the film fabricated at a T_{max} of 60 °C, suggesting that a lower T_{max}, besides developing a higher internal strain, also decreased the crystallite size. However, as confirmed by the ferroelectric hysteresis loops and emerging current peaks of E_B and E'_F (or E'_B and E_F) representing irreversible dipole rotation in the *I–E* loops shown in Fig. S5,† only if the requirements of high $F(\beta)$, small crystallite size, and high internal strain were simultaneously satisfied, stable relaxor-like ferroelectricity with low D_r and distinctive current peaks at high electric fields was able to be generated.

Guided by the results above, a new strategy with an annealing process at low temperature and high pressure was proposed to achieve a high $F(\beta)$, high internal strain, and good relaxor behaviour. The schematic diagram is presented in Fig. 2g. The rolled film was firstly pressed at 60 °C to promote sufficient stress transfer. The temperature was then increased to 165 °C, allowing a larger plastic deformation to achieve high $F(\beta)$. Subsequently, the film was quickly quenched with cold water to the annealing temperature T_{anneal} and kept for 10 minutes at this temperature to complete the internal strain build up and the transformation to a reversible polar nanostructure before the film was cooled down to the ambient temperature and the pressure was removed. As shown in Fig. 2h, i and S6b,† annealing at 60 °C not only boosted the internal strain to 5.9 ± 0.2% (calculated from the $(110)/(200)_\beta$ diffraction peak shift) compared with 2.1 ± 0.1% in the film prepared without low temperature annealing (or annealed at 165 °C) but also slightly enhanced the $F(\beta)$ from 90 ± 6% to 94 ± 3% with more uniform β-phase distribution over the whole film. Meanwhile, the crystallite size experienced a reduction to 4.1 ± 0.2 nm at a T_{anneal} of 60 °C. As shown in Fig. S7,† the Roll & Press and annealed PVDF displayed a similar melting temperature of ~172 °C to the hot-pressed PVDF film. Nevertheless, the calculated crystallinity (Table S3†) decreased from 46 ± 2% for the hot-pressed film to 44 ± 2% for the film Roll & Pressed and annealed at 165 °C, which was further reduced to 38 ± 1% for the film annealed at 60 °C, suggesting that the low T_{anneal} and high pressure suppressed the crystallization process.

The energy storage performance of a dielectric capacitor is mainly determined by the material's dielectric and ferroelectric behaviour at high electric fields, including the D_r, maximum field induced dielectric displacement $D_{in\text{-}max}$, the highest applied electric field E, and charge–discharge efficiency η (eqn (6)–(9) in the Experimental section). Compared with the Roll & Press film without annealing, the four highly stable current peaks $E_F(E'_F)$ and $E_B(E'_B)$ in the *I–E* loops for the annealed Roll & Press PVDF film at a high electric field of 640 kV mm^{-1} (Fig. 3b) confirmed the critical roles played by both the high internal strain and the high β-phase content, which promoted the transformation from irreversible to reversible polar nanostructures and is related to peaks for E_B and E'_B that are in the 2nd and 4th quadrants. The internal stress that is linked to the strain provided a driving force to reverse the electric field switched dipoles back to their original states after withdrawing the external fields, leading to a reduced D_r in the *D–E* loops (Fig. 3a) and an enhanced discharged energy density.[22] Unipolar *D–E* loops were obtained by applying two successive half-cycle triangular waveforms for 0.1 s to reveal the films' electrical properties during a fast charge–discharge process. As shown in Fig. S8a,† the D_r of the pristine 60 °C annealed Roll & Press film was further reduced to 0.009 C m^{-2} during the 2nd fast charge–discharge process (Fig. 3c) through suppressing ferroelectric switching from irreversible polar nanostructures (Fig. S8†). Therefore, a giant discharged energy density U_e of 50.2 J cm^{-3} was achieved, which is the highest ever obtained for any dielectric polymer or composite (Fig. 3d and f). The high-field efficiency η of the Roll & Press PVDF film exceeded 80% (Fig. 3d) owing to high reversible polar nanostructures, which is superior to all PVDF-based materials and even comparable with certain linear/dipolar glass polymers (Fig. 3d and f; Table S2†). One should note that the Roll & Press PVDF film exhibited a dielectric loss tan δ of 0.021 at 1 kHz and 25 °C, which is higher than that of the BOPP film (0.0002, at 1 kHz and 25 °C), but the low field dielectric loss (measured with an LCR meter) cannot be used to evaluate the dielectric loss of dielectrics under applied high field directly. For any dielectrics, higher field is related to higher dielectric loss. Unlike the low field dielectric loss which is constant during a measurement cycle,[32,33] high field dielectric loss varies with time during a test cycle due to field induced transitions.[34] Normally, the charge–discharge efficiency η of dielectrics is used to characterize the performance for high power energy storage.[8,10] One can directly use $1 - \eta$ to measure high field energy loss for high power energy storage applications. Under the same measurement conditions (unipolar *D–E* loop, 10 Hz, and room temperature), the high field charge–discharge efficiency η of Roll & Press PVDF (80% at 1000 kV mm^{-1}) is only slightly lower than that of BOPP (83% at 650 kV mm^{-1}).[7] In fact, the η of BOPP dramatically reduced from 98% at 400 kV mm^{-1} to 83% at 650 kV mm^{-1} while the Roll & Press PVDF showed a stable η of 80% from 600 kV mm^{-1} up to 1000 kV mm^{-1} (Fig. 3d).[7] Moreover, the U_e of Roll & Press PVDF (50.2 J cm^{-3} at 1000 kV mm^{-1}) is more than 12 times higher than that of BOPP (~4 J cm^{-3} at 650 kV mm^{-1}). As analysed using the two-parameter Weibull distribution and the experimental breakdown strength obtained during performing unipolar *D–I–E* loop measurement, the 60 °C annealed Roll & Pressed film (thickness: 10–20 μm) demonstrated a characteristic breakdown strength E_b of 904 kV mm^{-1} (U_e: 42.2 J cm^{-3}) with a high reliability factor β of 12.7 (Fig. 3e), ensuring that the film exhibited not only high U_e but also high reliability during its service at high fields. Such a high breakdown strength of PVDF correlates with the outstanding film quality and enhanced mechanical strength after Roll & Press. On one hand, the one-step processing method at high pressure significantly reduced the possibility of introducing extrinsic defects (*e.g.*, dust, moisture, impurities, voids, *etc.*) into the film and enhanced the film quality compared with Press & Fold where multiple processing steps are involved. As a result, the probability of electrical treeing, which normally initiates at weak points, is also reduced. Secondly, after compressing at high pressure, the pre-strained Roll & Press PVDF film with local stress enhancement should be mechanically stronger and

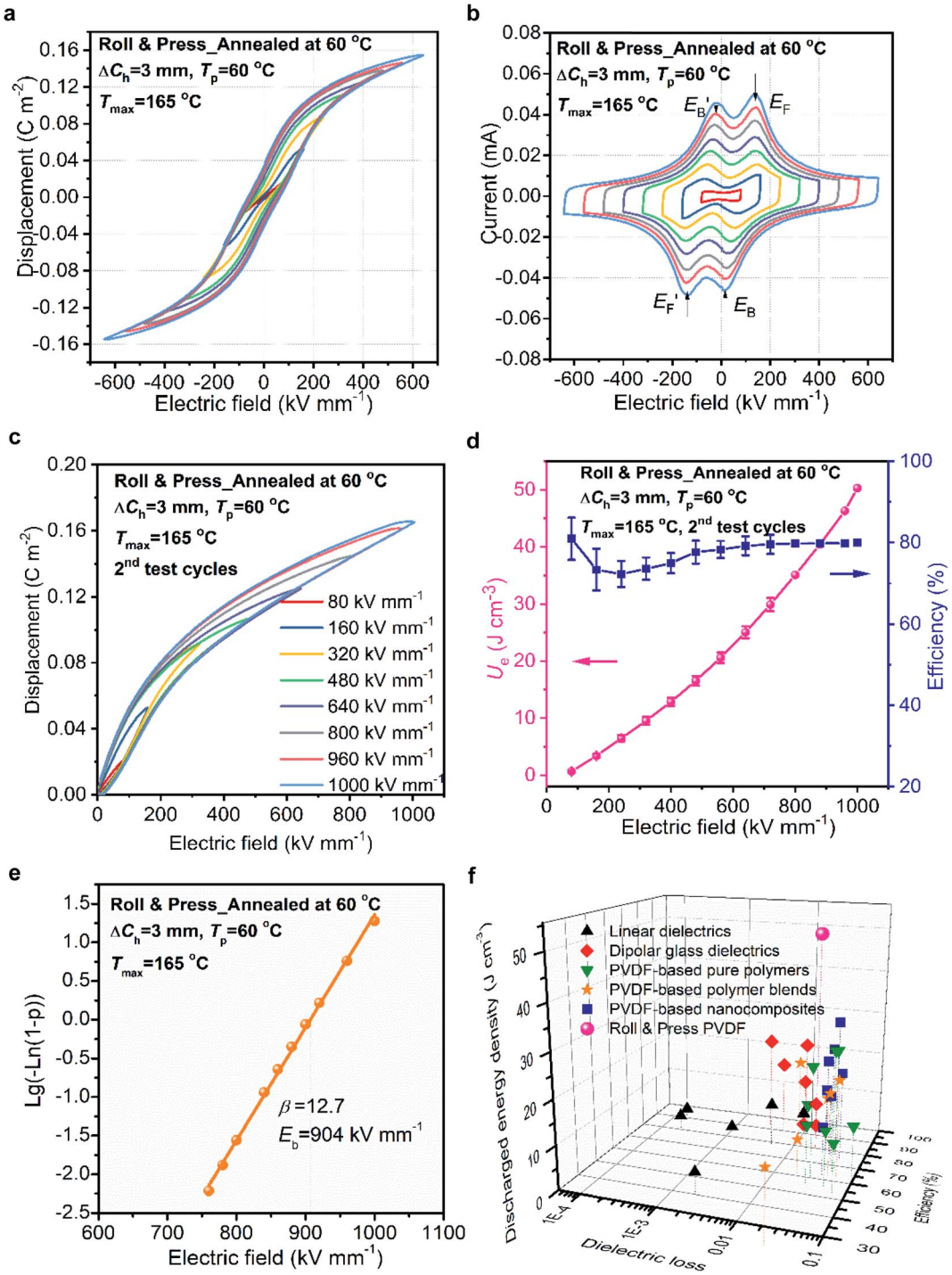

Fig. 3 a) Bipolar D–E loops; (b) bipolar I–E loops; (c) unipolar D–E loops; (d) U_e and η; (e) Weibull analysis of the dielectric breakdown strength of the 60 °C annealed Roll & Press film with a ΔC_h of 3 mm. (As restricted by the different breakdown fields of 10 samples, data below 720 kV mm^{-1} are means ± standard deviations (if applicable) obtained based on 10 results. Data above 720 kV mm^{-1} were obtained from the sample with a breakdown strength of 1000 kV mm^{-1}). (f) Discharged energy density comparison of current available polymers for dielectric energy storage applications (summarized and referred to Table S2†).

display higher Young's modulus compared to non-strained PVDF films prepared by solution casting or hot pressing. This is confirmed by our previous study on the pre-strained Press & Fold PVDF film, where a higher Young's modulus of 1800 MPa was measured in PVDF after 6 Press & Fold cycles compared to 1450 MPa of hot-pressed PVDF.[22] The enhanced mechanical strength is also beneficial for enhancing the breakdown strength by reducing the probability of electromechanical breakdown according to the Stark–Garton model.[35] In addition, the energy storage properties of the Roll & Press film exhibited

high homogeneity over the entire film (~300 cm^2) at similar electric fields regardless of the selected testing area because of the uniform microstructure and reversible polar nanostructure distribution under given processing conditions.

In addition to the record high electrical properties presented above, the novel method of Roll & Press is a potentially disruptive technology, providing the possibility of simultaneously incorporating electrodes, hence fabricating a performing film capacitor in one step. Traditionally, polymer film capacitors are prepared by a process of winding a dielectric film along with a continuous metal electrode. The Roll & Press process can be modified by inserting an electrode layer, without interfering with the bespoke thermomechanical treatment of the PVDF film, which is necessary to achieve high $F(\beta)$ and high internal strain to induce stable relaxor-like ferroelectricity. As a proof of concept, we now demonstrated that this is possible by using a carbon nanotube veil (CNT veil) layer as electrodes. PVDF with a CNT veil was assembled by Roll & Press ($T_p = 60$ °C and $T_{max} = 165$ °C), followed by annealing at high temperature ($T_{anneal} = 165$ °C) and low temperature ($T_{anneal} = 60$ °C). As presented in Fig. 4a, the CNT veil presented a microscopic preferred orientation and a robust network that ensured that electrical conductivity was not significantly affected even after pressures as high as 300 MPa were applied. Although the conductivity of the CNT veil decreased from 25.3 ± 4.8 S cm^{-1} to 14.8 ± 3.7 S cm^{-1} after Roll & Press, this level of electrical conductivity is still high enough to produce good results as electrodes for high field measurements. As shown in Fig. S10,† the electrode film annealed at 60 °C contained more than 95 ± 3% of β phase. The *D–I–E* loops of the as-prepared capacitors were tested to confirm their high-field behaviours (Fig. 4b and c; S11†). It was found that the capacitors fabricated with low-temperature annealing treatment also displayed four stable current peaks in four quadrants in the *I–E* loops and slim *D–E* loops with a D_r of 0.032 C m^{-2} and $D_{in\text{-}max}$ of 0.109 C m^{-2}, leading to a recoverable energy storage density U_e of 5.8 J cm^{-3} at 240 kV mm^{-1}, which is higher than that of the capacitor annealed at high temperature ($T_{anneal} = 165$ °C) (Fig. S12†) and congruent with the Roll & Press PVDF films presented before. In addition, adding the CNT veil layer does not affect the stretchability and processability of the PVDF film. According to the sample dimension changes before and after Roll & Press under

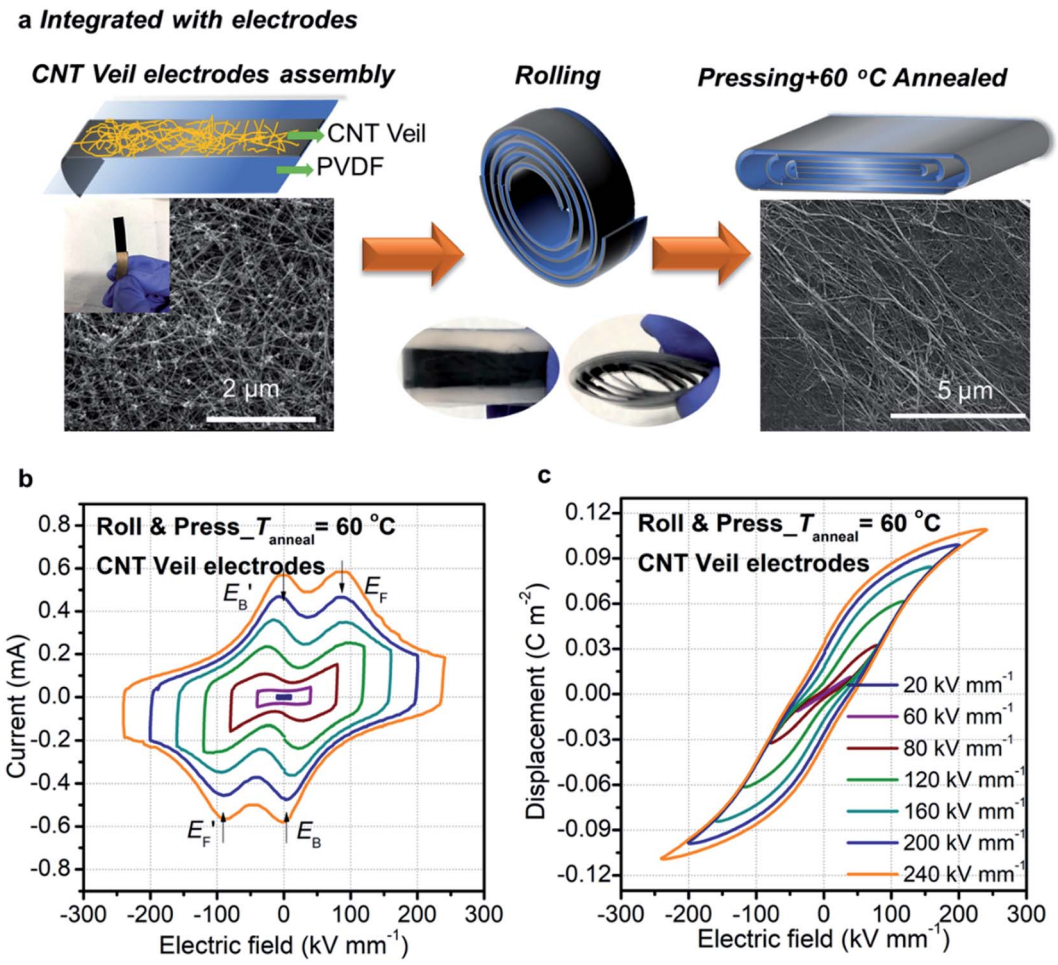

Fig. 4 a) Scheme of the one-step fabrication process for dielectric capacitors with integrated CNT veil electrodes using Roll & Press. The SEM images show the surface morphology of the pristine CNT veil and the CNT veil after Roll & Press under a pressure of 300 MPa. (b) *D–E*; (c) *I–E* loops of the prepared capacitor with electrodes ($T_p = 60$ °C, $T_{max} = 165$ °C, and $T_{anneal} = 60$ °C) as a function of applied fields.

optimum processing conditions ($\Delta C_h = 3$ mm, $T_p = 60$ °C, $T_{max} = 165$ °C, and $T_{anneal} = 60$ °C), both the Roll & Press PVDF with and without the CNT veil layer exhibited a similar film area increase (~5.2 times compared to the film before pressing). These results indicate that the single step Roll & Press with embedded electrodes is a feasible and promising approach for manufacturing next generation dielectric capacitors with high energy density. However, the breakdown strength of the one-step assembled dielectric capacitor with a CNT veil is lower than that of silver coated ones. This could be attributed to the penetration of soft conductive carbon nanotubes into the PVDF film during pressing, which enhances charge injection and makes the conductive pathway easier to form at high fields across the PVDF film. The results can potentially be improved by replacing the soft carbon nanotubes with rigid metal nanowire/nanofibers or inserting a metal-based conductive network between the PVDF and the CNT veil to fabricate a double layer electrode in future studies.

3. Conclusions

In conclusion, we demonstrated a novel one-step approach, "Roll & Press", for fabricating high power density dielectric capacitors with outstanding discharged energy density and efficiency. Under optimised conditions ($\Delta C_h = 3$ mm, $T_p = 60$ °C, $T_{max} = 165$ °C, and $T_{anneal} = 60$ °C), a high fraction of β-phase ($94 \pm 3\%$) with nano-sized crystallites (4.1 ± 0.2 nm) and high internal lattice strain ($5.9 \pm 0.2\%$) was achieved in Roll & Press PVDF, which led to a record energy density of 50.2 J cm^{-3} with a charge–discharge efficiency of 80% achieved at a breakdown strength of 1000 kV mm^{-1}. Various multilayer structures were investigated to reveal the effect of boundary conditions on the phase transformation efficiency and ferroelectric properties. It was proved that the desirable properties are associated with the constraining effect induced by the continuous folded boundaries that are introduced during the rolling process, which leads to a high β phase content (>90%) with all-trans chain conformation. The high internal strain (~5.9%) drives the reverse switching of the polar nanodomains after withdrawing the external field, leading to a relaxor-like behaviour. Our results show that high fraction of β phase, small crystallite size, and high internal strain are essential for inducing a reversible polar nanostructure, reducing high-field energy loss, and enhancing energy storage density in PVDF. A ready-to-use capacitor was also demonstrated by rolling & pressing a PVDF film with a carbon nanotube veil flexible electrode, which exhibited comparable high-field properties to post silver sputtered PVDF films, making this approach available for potential large-scale production for developing future capacitors.

4. Experimental section

4.1 Materials

Homopolymer PVDF powder (M_w: 670–700 kg mol^{-1}) was purchased from Solvay. The carbon nanotube veil (CNT veil) was kindly supplied by the Suzhou Institute of Nano-Tech and Nano-Bionics (SINANO), China. All the materials were used as received.

4.2 Film fabrication and dielectric capacitor assembly

Hot-pressed PVDF films were prepared using a Dr Collin hot press machine P300E (Dr COLLIN GmbH, Germany). The PVDF powder was melted at 180 °C and pressed with a force of 150 kN for 5 minutes and then quenched with cold water to obtain the initial film with a thickness of ~150–250 μm (final pressure: ~20 MPa). Rectangular shape films (25 cm × 4 cm) were cut from the hot-pressed film to make multilayer structures. The 10-layer films (2.5 cm × 4 cm for each layer) with a final area of 10 cm^2 were assembled *via* three different approaches: "Stack & Press", "Zigzag & Press" and "Roll & Press" (Fig. 1a). The assembled multilayer films were pressed with a force of 300 kN (pressure = 300 kN/10 cm^2 = 300 MPa) at $T_p = 60$ °C. The temperature was then increased to $T_{max} = 165$ °C. After reaching T_{max}, the films were quenched with cold water to the pre-set T_{anneal} and maintained at the same temperature and pressure for 10 minutes to promote the phase transformation from the α to the β phase and internal stress accumulation. Finally, the films were quenched with cold water to ambient temperature and the pressure was removed. The different rolling strategies (tightly rolled and loosely rolled) were adopted to understand the influence of the boundary conditions. ΔC_h is used to clarify different rolling scenarios, which is defined as the difference of circumferences between the current semicircle and the previous semicircle during rolling. The length of each layer and the difference of ΔC_h were measured and marked on the films before rolling. When the film was rolled, the marked lines were aligned to ensure that the ΔC_h was consistent in the whole film. A series of T_p, T_{max} and T_{anneal} were selected to reveal the effect of temperature. A thin layer of the CNT veil was attached to the top side of the hot-pressed PVDF and then Roll & Press using a similar procedure to complete the integration of the electrodes.

4.3 Microstructure characterization

The morphology of the film surfaces was studied using a scanning electron microscope (SEM) (FEI Inspect-F, USA). The chain conformations and crystalline phase compositions of PVDF were examined using a Fourier transform infrared spectrometer (FTIR) Tensor 27 in ATR mode (Bruker Optik GmbH, Germany). As only α and β phases exist in the pressed PVDF films according to the representative FTIR peaks, the fraction of β phase $F(\beta)$ was calculated based on the Beer–Lambert law, $F(\beta) = \frac{A_\beta}{1.26A_\alpha + A_\beta}$ (eqn (1)), where A_α and A_β are the absolute intensities of peaks at 762 cm^{-1} and 840 cm^{-1}, respectively. The results presented in this work are based on 10 measurements. X-ray diffraction (XRD) patterns were acquired from 5–70° 2θ using an X'Pert Pro diffractometer with Cu-Kα radiation (PANalytical, Netherlands) to confirm the phase composition obtained from FTIR and provide more information on the crystallite size and internal strain. Deconvolution was performed for the experimentally measured XRD patterns to

differentiate overlapped diffraction peaks. The average crystallite size (lamellae thickness) along the (*hkl*) crystal plane was roughly estimated according to Scherrer's equation, $D_{hkl} = \frac{K\lambda}{\beta_{hkl}\cos\theta}$ (eqn (2)), in which K is the shape factor (0.89 is chosen in this case), λ is the wavelength of the incident X-ray (λ = 0.15418 nm), β_{hkl} is the full width of half maximum along the (*hkl*) direction, and θ is the diffraction angle. The interchain distance was given by Bragg's law, $2d\sin\theta = n\lambda$ (eqn (3)). The internal lattice strain ε was calculated using $\varepsilon = \frac{d_1 - d_0}{d_0}$ (eqn (4)), where d_1 and d_0 are the interchain distance of the $(200)/(110)_\beta$ crystal plane for the roll-pressed PVDF and the annealed stress-free PVDF, respectively.[22] Thermal analysis was conducted using a DSC 25 (TA Instruments, Belgium) to study the thermal behaviour. Samples with an average weight of 5 mg were tested between −40 °C and 200 °C with a heating rate of 10 °C min^{-1}. The fusion enthalpy ΔH_m was acquired by integrating the area of the melting peak during the first heating cycle. The crystallinity χ_c was estimated using $\chi_c = \frac{\Delta H_m}{\Delta H_{m\text{-}100\%}} \times 100\%$ (eqn (5)), where the $\Delta H_{m\text{-}100\%}$ is 104.0 J g^{-1}, which is the fusion enthalpy of the 100% crystalline of PVDF. The results presented in this work are based on 3 measurements.

4.4 FEM simulation

The three different pressing modes have been simulated using commercial FE software ABAQUS. The models aim at clarifying how the different configurations affect the local plastic deformation in the vicinity of the folded boundaries. The main difference among them lies in the geometry of the boundaries. Therefore, the three models simulate sections of two half-layers for each film. Half-layers are enough to describe the mechanics of the films due to their symmetry.

The material response under compression was extracted from the experimental data of a PVDF layer, and a non-linear plastic deformation follows an initial linear elastic behavior (Fig. S13†). Therefore, the Young's modulus, yield stress, and plastic strains (elastic–plastic response) were defined in order to reproduce the collected experimental data.

Displacement boundary conditions are set for the two press plates, which were modelled as rigid solids. The friction coefficient was set equal to 0.2 for the plate-PVDF contact surface and equal to 0.3 for the PVDF–PVDF contact surface. Explicit dynamic simulations have been performed using a mesh consisting of four-node plane stress elements with reduced integration (CPS4R), and a convergent behavior was obtained using six elements across the thickness of each layer. Quasi-static conditions were ensured by checking that the kinetic energy during the simulations was less than 0.5% of the total energy. An adaptive mesh was used to overcome mesh distortion.

4.5 Dielectric and ferroelectric property characterization

Silver electrodes were sputtered on both sides of the prepared PVDF films using an Agar Automatic Sputter Coater (Agar Scientific, UK) in an argon atmosphere with the current control at 30 mA for 9 minutes. The approximate thickness of the coated electrode is 100 nm. The diameter of the electrode for dielectric and ferroelectric property measurements was 5 mm and 2 mm, respectively. The temperature dependent low-field dielectric properties were measured using a LCR meter (Agilent 4284A, USA) connected to a homemade furnace within the temperature range of –50–150 °C and the frequency range of 100–100 kHz. The temperature ramp rate was 3 °C min^{-1}. The ferroelectric properties were characterized using displacement–current–electric field (*D–I–E*) loops acquired using a ferroelectric hysteresis loop measurement system (National Physics Laboratory, UK) at room temperature and 10 Hz. Both bipolar and unipolar loops were measured using full-cycle triangular waveforms and half-cycle triangular waveforms, respectively. To make sure that the data are reliable and representative in our work, we adopted two measures. On the one hand, to eliminate the errors caused by inaccurate dimension measurement, the diameter of the electrodes was controlled using a mask and the thickness was measured several times using a digital micrometre to obtain an average thickness. On the other hand, we cut 20 samples from different areas of a large film (~300 cm^2) and then randomly selected 10 of them to perform tests to ensure the randomness. The discharge energy density U_e during the depolarisation process was calculated by integrating the discharge curves in the unipolar *D–E* loops using $U_e = \int_{D_{in\text{-}max}}^{D_r} E\mathrm{d}D$ (eqn (6)), where D_r is dielectric displacement at zero field and $D_{in\text{-}max}$ is the maximum electric field induced dielectric displacement. The total charged energy during the polarisation process was calculated using $U_t = \int_0^{D_{in\text{-}max}} E\mathrm{d}D$ (eqn (7)).[10,34] The charge–discharge efficiency was calculated using $\eta = \frac{U_e}{U_t} \times 100\ \%$ (eqn (8)). The characteristic breakdown strength E_b at which the probability of dielectric breakdown is 63.2% was calculated using the two-parameter Weibull distribution, $P(E) = 1 - \exp[-(E/E_b)^\beta]$ (eqn (9)), where the E is the experimentally measured breakdown field, $P(E)$ is the statistic cumulative probability of dielectric breakdown and β is the reliability parameter. Other than the DC approach with a slow linear field ramp rate, the breakdown field in this work was measured using a ferroelectric hysteresis loop testing system with a fast charge–discharge speed (0.1 s) by increasing the applied field by 40 kV mm^{-1} each time until the breakdown occurred. 10 samples were measured until breakdown to provide the experimental breakdown field E.

Conflicts of interest

There are no conflicts to declare.

Acknowledgements

This work is sponsored by the Shanghai Pujiang Program (20PJ1400600) and National Natural Science Foundation of China (52103024). The authors appreciate the Suzhou Institute of Nano-Tech and Nano-Bionics (SINANO), China for providing

the carbon nanotube veil for this research work. Xintong Ren (CSC No.: 201606280030) would like to thank the China Scholarship Council for the financial support.

References

1 E. Baer and L. Zhu, *Macromolecules*, 2017, **50**, 2239–2256.
2 Z.-M. Dang, J.-K. Yuan, S.-H. Yao and R.-J. Liao, *Adv. Mater.*, 2013, **25**, 6334–6365.
3 Q. Chen, Y. Shen, S. Zhang and Q. M. Zhang, *Annu. Rev. Mater. Res.*, 2015, **45**, 433–458.
4 Prateek, V. K. Thakur and R. K. Gupta, *Chem. Rev.*, 2016, **116**, 4260–4317.
5 E. J. Barshaw, J. White, M. J. Chait, J. B. Cornette, J. Bustamante, F. Folli, D. Biltchick, G. Borelli, G. Picci and M. Rabuffi, *IEEE Trans. Magn.*, 2007, **43**, 223–225.
6 X. Yuan, Y. Matsuyama and T. C. M. Chung, *Macromolecules*, 2010, **43**, 4011–4015.
7 Q. Chen, Y. Wang, X. Zhou, Q. M. Zhang and S. Zhang, *Appl. Phys. Lett.*, 2008, **92**, 142909.
8 H. Pan, F. Li, Y. Liu, Q. Zhang, M. Wang, S. Lan, Y. Zheng, J. Ma, L. Gu, Y. Shen, P. Yu, S. Zhang, L.-Q. Chen, Y.-H. Lin and C.-W. Nan, *Science*, 2019, **365**, 578–582.
9 B. Chu, X. Zhou, K. Ren, B. Neese, M. Lin, Q. Wang, F. Bauer and Q. M. Zhang, *Science*, 2006, **313**, 334–336.
10 L. Yang, X. Kong, F. Li, H. Hao, Z. Cheng, H. Liu, J.-F. Li and S. Zhang, *Prog. Mater. Sci.*, 2019, **102**, 72–108.
11 T. Furukawa, *PTMJ*, 1989, **18**, 143–211.
12 A. J. Lovinger, *Science*, 1983, **220**, 1115–1121.
13 P. Martins, A. C. Lopes and S. Lanceros-Mendez, *Prog. Polym. Sci.*, 2014, **39**, 683–706.
14 Z. Zhang, X. Wang, S. Tan and Q. Wang, *J. Mater. Chem. A*, 2019, **7**, 5201–5208.
15 K. L. Kim, W. Lee, S. K. Hwang, S. H. Joo, S. M. Cho, G. Song, S. H. Cho, B. Jeong, I. Hwang, J.-H. Ahn, Y.-J. Yu, T. J. Shin, S. K. Kwak, S. J. Kang and C. Park, *Nano Lett.*, 2016, **16**, 334–340.
16 C. Ribeiro, C. M. Costa, D. M. Correia, J. Nunes-Pereira, J. Oliveira, P. Martins, R. Gonçalves, V. F. Cardoso and S. Lanceros-Méndez, *Nat. Protoc.*, 2018, **13**, 681–704.
17 W. Li, Q. Meng, Y. Zheng, Z. Zhang, W. Xia and Z. Xu, *Appl. Phys. Lett.*, 2010, **96**, 192905.
18 N. Meng, X. Ren, G. Santagiuliana, L. Ventura, H. Zhang, J. Wu, H. Yan, M. J. Reece and E. Bilotti, *Nat. Commun.*, 2019, **10**, 4535.
19 F. Guan, J. Pan, J. Wang, Q. Wang and L. Zhu, *Macromolecules*, 2010, **43**, 384–392.
20 F. Guan, J. Wang, J. Pan, Q. Wang and L. Zhu, *Macromolecules*, 2010, **43**, 6739–6748.
21 L. Yang, X. Li, E. Allahyarov, P. L. Taylor, Q. M. Zhang and L. Zhu, *Polymer*, 2013, **54**, 1709–1728.
22 X. Ren, N. Meng, H. Zhang, J. Wu, I. Abrahams, H. Yan, E. Bilotti and M. J. Reece, *Nano Energy*, 2020, **72**, 104662.
23 Y. Huang, G. Rui, Q. Li, E. Allahyarov, R. Li, M. Fukuto, G.-J. Zhong, J.-Z. Xu, Z.-M. Li, P. L. Taylor and L. Zhu, *Nat. Commun.*, 2021, **12**, 675.
24 H. Lu, J. Du, C. Yu, X. Wang, Y. Gao, W. Xu, A. Liu, X. Lu and Y. Chen, *Macromolecular Research*, 2020, pp. 1–7.
25 Y. Ting, C. W. Chiu and H. Gunawan, *J. Appl. Polym. Sci.*, 2018, **135**, 46677.
26 S. Qu, X. Jiang, Q. Li, L. Gao, G. Zhou, D. Zhang, W. Gong and W. Lu, *Carbon*, 2019, **149**, 117–124.
27 K. Jiang, Q. Li and S. Fan, *Nature*, 2002, **419**, 801.
28 V. Sencadas, R. Gregorio and S. Lanceros-Méndez, *J. Macromol. Sci., Part B: Phys.*, 2009, **48**, 514–525.
29 R. Gregorio and E. M. Ueno, *JMatS*, 1999, **34**, 4489–4500.
30 R. Hasegawa, M. Kobayashi and H. Tadokoro, *Polym. J.*, 1972, **3**, 591–599.
31 J. Defebvin, S. Barrau, G. Stoclet, C. Rochas and J.-M. Lefebvre, *Polymer*, 2016, **84**, 148–157.
32 *ASTM D150-18: Standard Test Methods For AC Loss Characteristics And Permittivity (Dielectric Constant) Of Solid Electrical Insulation*, 2018.
33 M. W. Barsoum, *Fundamentals of ceramics*, CRC press, 2019.
34 J. Wu, A. Mahajan, L. Riekehr, H. Zhang, B. Yang, N. Meng, Z. Zhang and H. Yan, *Nano Energy*, 2018, **50**, 723–732.
35 K. H. Stark and C. G. Garton, *Nature*, 1955, **176**, 1225–1226.

